Effect of reinforcement connectivity on the elasto-plastic behavior of aluminum composites containing sub-micron alumina particles

M. Kouzeli, D.C. Dunand *

Department of Materials Science and Engineering, Northwestern University, 2220 Campus Drive, Evanston, IL 60208, USA

Abstract

The mechanical properties of composites consisting of an aluminum matrix with 34 and 37 vol.% sub-micron Al_2O_3 particles were studied in compression for two reinforcement architectures: interconnected and discontinuous. Both the elastic and plastic behaviors of these composites are successfully modeled using a self-consistent approach: the classical self-consistent and the three-phase self-consistent models for the interconnected and discontinuous architectures, respectively. At ambient temperature, an interconnected architecture offers only a modest increase in stiffness and strength over a discontinuous architecture of equal volume fraction. At elevated temperatures (250, 500 and 600 °C), the interconnected reinforcement becomes increasingly more effective at strengthening the composites. However, the relative increase in strength due to interconnectivity can only be exploited at small strains (1–5%) due to the early development of compressive flow instabilities in the interconnected composites. While microstructural damage controls the instability strain of the interconnected composites at ambient temperature, their low strain-hardening coefficient is the main contribution to flow instabilities at elevated temperature.
© 2003 Acta Materialia Inc. Published by Elsevier Ltd. All rights reserved.

Keywords: Particulate reinforced composites; Aluminum; Interpenetrating microstructure; Compression test; Mean field analysis

1. Introduction

The shape and spatial arrangement of the reinforcing phase in metal matrix composites are key parameters in determining their mechanical behavior [1]. In Discontinuously Reinforced Composites (DRCs), the link between reinforcement morphology and macroscopic composite behavior has been explored both experimentally and theoretically, allowing for the identification of critical reinforcement characteristics, e.g. aspect ratio and angularity [2,3]. The topological attributes of the reinforcement, on the other hand, have not been as systematically studied, primarily due to the difficulty in controlling the spatial arrangement of the reinforcement during processing. Reinforcement clustering, an undesirable result of processing, is, thus, the most studied aspect of reinforcement topology in DRCs, e.g. [4,5].

---

* Corresponding author. Tel.: +1-847-491-5370; fax: +1-847-467-6573.
E-mail address: dunand@northwestern.edu (D.C. Dunand).

Recently, a different topological feature of the reinforcement has been considered, i.e. its connectivity or contiguity. In commercially produced DRCs, each particle is surrounded by a continuous layer of metal matrix. Novel processing techniques have made it possible to produce composites in which both metal and ceramic phases are continuous and interpenetrating throughout the microstructure [6–8]. These Interpenetrating Phase Composites (IPCs), which are also referred to as co-continuous [8], bi-continuous [9], and C^4 composites [10], have been studied ever since it was postulated that an interpenetrating microstructure could improve the physical and mechanical properties of composite materials [6].

Most experimental studies on IPCs, however, have focused on systems in which the ceramic is the majority phase by volume [7,10–14]. In these interpenetrating-phase ceramic-matrix composites, the metal acts primarily as a toughening agent for the ceramic matrix; the toughness and strength of such IPCs have been explicitly correlated to the thickness and volume fraction of the metal ligaments in their microstructure. Whether or not the interpenetrating topology is beneficial to the mechanical properties of the ceramic-matrix IPCs has not been put into evidence, however, since the effects of interpenetration have not been isolated.

Numerical simulations have also been carried out recently to study the effects of interpenetrating microstructures in composite materials [15]. The results of these calculations, conducted using finite element analysis, indicate that the interconnectivity of the constituent with the most desired properties imparts improved properties to the composite, as opposed to the interpenetrating microstructure itself. Experimental studies were carried out in parallel to these simulations, and reasonable agreement between the measured and predicted properties of those IPCs (sintered stainless steel preforms infiltrated with either bronze or epoxy) was achieved [16,17]. While the theoretical part of the study addressed the difference in behavior between composites with similar microstructures, one of which is interpenetrating and the other not, the experimental part did not directly isolate the effect of interpenetration by comparing such materials.

The purpose of the present study is to fill two

gaps in the literature of IPCs. First, we explore the elasto-plastic properties of Al–Al$_2$O$_3$ IPCs, in which the metal phase is the majority phase and the stiff ceramic phase a reinforcement. In addition, we compare two similar composite microstructures, one of which is interpenetrating (IPC) and the other not (DRC), so as to experimentally establish the role of reinforcement interconnection in a directly observable manner. We demonstrate that interconnection between individual ceramic reinforcing particles affects the mechanical behavior in these Al–Al$_2$O$_3$ composites, and we quantify this effect. We also show that two analytical models—the classical self-consistent (CSC) approach and the three-phase self-consistent (3PSC) approach—can be used successfully to predict the elasto-plastic behavior of these IPCs and DRCs, respectively.

2. Experimental procedures

Chesapeake Composites Corp. (New Castle, DE) supplied dispersion-strengthened cast aluminum (DSC-Al™), an Al–Al$_2$O$_3$ composite produced by liquid–metal infiltration. In this process, self-supporting Al$_2$O$_3$ preforms are prepared by spray-drying a slurry of equiaxed Al$_2$O$_3$ particles with an average diameter of 0.3 μm, followed by partial sintering [18]. The ceramic preforms are then pressure-infiltrated with commercial-purity aluminum to produce a fully dense Al–Al$_2$O$_3$ composite. As-cast DSC-Al is an IPC due to its interpenetrating metal-ceramic microstructure. DRCs can be obtained from the as-cast composites by an extrusion process, which breaks up the network of reinforcement without introducing measurable porosity. Three DSC-Al billets were used in this study: two with 34 vol.% Al$_2$O$_3$ (referred to as IPC34), the third nearly identical but with 37 vol.% Al$_2$O$_3$ (referred to as IPC37). One of the IPC34 castings was extruded at 500 °C with an extrusion ratio of 12:1, and is referred to in the following as DRC34. Chesapeake Composites Corp. also supplied an uninfiltrated Al$_2$O$_3$ preform identified as PA34, with the same volume fraction of Al$_2$O$_3$ as IPC34 and DRC34.

Optical microscopy and scanning electron microscopy (SEM) were used to characterize the

microstructures of the composites in the as-received state and after mechanical testing. For SEM imaging, mechanical polishing was followed by an electro-polishing step (3 s at 50 V with Struers A2 electrolyte) in order to preferentially remove a layer of aluminum and reveal the reinforcement architecture within the composites. In deformed specimens, the electro-polishing step also helped to reveal any voids within the matrix of the composites produced during straining, which were not discernable after simple mechanical polishing due to smearing of the soft aluminum matrix. Helium pycnometry was employed in determining the density of the composites. Volume fractions of ceramic in the composites were determined from these density measurements assuming no porosity and densities for bulk Al_2O_3 and Al of 3.97 and 2.698 g/cm^3, respectively.

Compressive testing was conducted on cylindrical samples 10 mm in diameter and 15 mm in height, with the long dimension of the samples coinciding with the infiltration direction and the extrusion direction for IPC and DRC materials, respectively. The samples were uniaxially compressed between polished WC/Co platens in a 100 kN servo-hydraulic universal testing machine outfitted with a controlled-atmosphere chamber and a furnace. Teflon was used as a lubricant between the sample and the platen surfaces for temperatures up to 250 °C, while BN was used at higher temperatures. For all experiments at elevated temperature, the testing chamber was first evacuated and flushed with Ar to avoid oxidation of the WC/Co platens, then heated at 10 °C/min to the specific testing temperature and left to equilibrate for 45 min prior to testing. The rate of cooling of the chamber after testing was the same as the heating rate. The compressive behavior of the IPCs was determined at 25, 250, 500, 600, 670 and 720 °C, while DRC34 and PA34 were tested at 25, 500, and 670 °C. Deformation was conducted under constant crosshead displacement at an initial strain-rate of 10^{-3} s^{-1}, with the measured strain rates throughout a single test never varying by more than a factor of 1.3. Strain in the samples was determined from the crosshead displacement, corrected for the (temperature-dependent) compliance of the testing set-up.

The effect of pre-straining at a temperature different from the testing temperature was determined on IPC34. Pre-straining temperatures both higher and lower than the testing temperature were used, i.e. pre-straining at 500 °C, followed by testing at each 25, 250, and 670 °C, as well as pre-straining at 25 °C, followed by testing at 250 °C. The strain increment applied during the pre-straining step approximately equaled the strain at maximum stress at the specific temperature.

The elastic constants of the composites were determined using an ultrasonic wave reflection technique on compression specimens prior to mechanical testing. The longitudinal and transverse speeds of sound were measured using two 50 MHz transducers linked to a digital oscilloscope. Molasses was employed as a coupling agent between the transducers and the sample. From these two speeds and the measured density of each sample, the Young's modulus and Poisson's ratio of the composites were determined [19]. Ultrasonic measurements were also used to determine the evolution of the Young's modulus (in the direction of loading) and Poisson's ratio (perpendicular to the direction of loading) as a function of compressive strain. The specimens were compressed to a pre-defined strain, unloaded and cooled if necessary, and then subjected to the ultrasonic measurements at room temperature. This procedure was repeated several times for each sample, at increasing strains. The density of the samples was also measured after each straining increment, to account for any density changes in the determination of the elastic constants [19]. The evolution of the elastic constants was determined for samples tested at 25, 250 and 500 °C for IPC34, at 25 and 500 °C for DRC34, and at 25 °C for IPC37.

3. Results

3.1. Composite microstructure

The microstructure of IPC37, IPC34 and DRC34, is characterized by a near-homogeneous distribution of sub-micron alumina particles in a pore-free aluminum matrix, as illustrated in the

optical micrographs of Fig. 1a and b. Unlike the DRC, the IPCs exhibit slight microstructural inhomogeneities in the form of spherical, alumina-rich regions between 10 and 100 μm in diameter that are surrounded by narrow channels of nearly pure aluminum matrix (Fig. 1a); these spheres are probably a product of spray-drying the alumina slurry during preform preparation [18]. Fig. 1c is a SEM micrograph of IPC34 after electro-polishing, which removed the aluminum matrix while leaving the three-dimensional reinforcement structure unaffected; the interconnected nature of the Al_2O_3 reinforcement is apparent. Fig. 1c also illustrates that the alumina particles did not significantly coarsen during sintering, as their shape and size (0.3 μm) are similar to those of the initial particles.

The integrity of the alumina network was determined by dissolving the aluminum matrix from several composite samples in a concentrated NaOH:KOH solution. After dissolution of the matrix from a DRC34 sample, only a fine slurry of particulate remained. In contrast, when the metal was dissolved from a sample of IPC34, an interconnected skeleton remained that could be handled without damaging it, and loose powder was not observed in the caustic solution. Clearly, the infiltration process does not significantly damage the continuous nature of the alumina preform, while the extrusion process reduces the alumina network to discrete and discontinuous particulates.

3.2. Elastic constants

Values for the elastic constants determined by ultrasonic measurements are listed in Table 1; these values are averages of measurements on different samples of the same material. IPC34 has a larger Young's modulus and smaller Poisson's ratio than DRC34. The relative increase in stiffness due to interconnectivity of the reinforcement is 9% for 34 vol.% Al_2O_3. Increasing the volume fraction of alumina in the IPCs also results in a stiffness increase and Poisson's ratio decrease, as evidenced in the comparison of IPC34 and IPC37 in Table 1; the difference in Poisson's ratio, however, is not statistically significant.
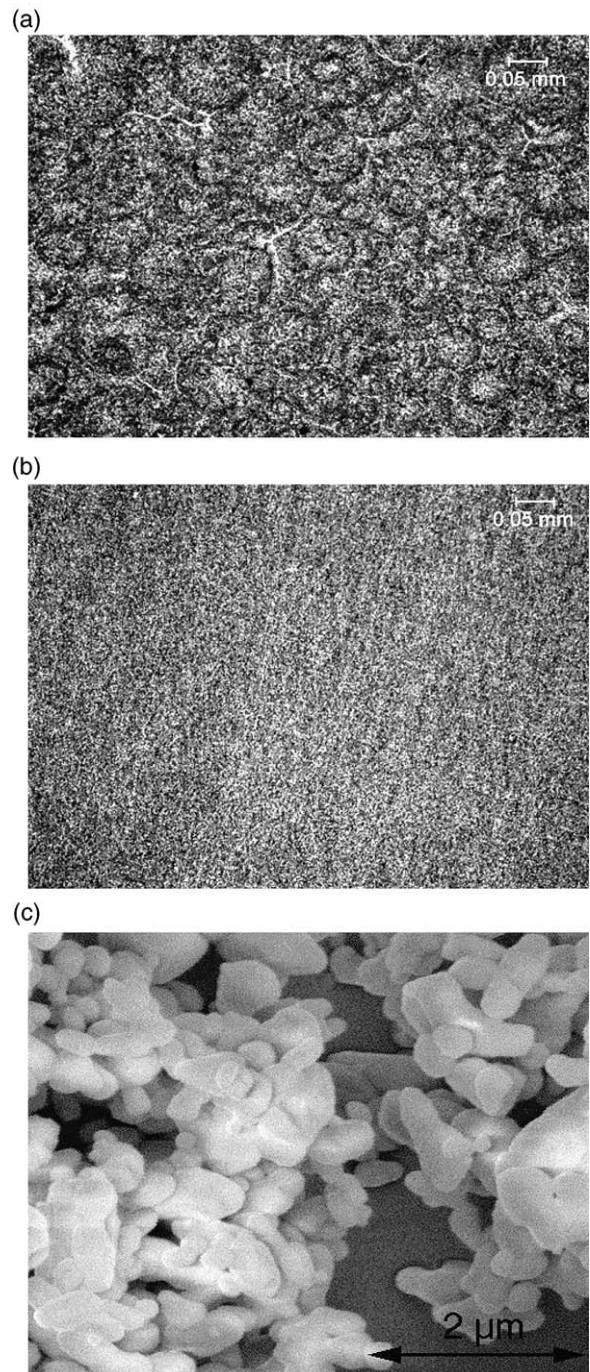

Fig. 1. Optical micrographs of (a) IPC34 and (b) DRC34; the light gray phase is Al and the dark gray Al_2O_3. (c) SEM micrograph of electropolished IPC34 where the lighter phase is the Al_2O_3 and the darker phase is the Al. The samples are not deformed.

Table 1
Measured elastic constants

	E_0 (GPa)	ν
DRC34	116 ± 2	0.320 ± 0.005
IPC34	127 ± 2	0.297 ± 0.005
IPC37	135 ± 2	0.295 ± 0.005

3.3. Compressive behavior

Typical compressive flow curves of the composites for various testing temperatures are given in Fig. 2. Table 2 summarizes the results of the compression tests in terms of the peak stress, σ_{max}, and the flow stress at a reference strain of 1%, $\sigma_{1\%}$, both of which are averages of at least three samples tested. In this paper, true stress and true strain values are reported for the composites, and nominal stress values are reported for the preform PA34, i.e. the stress calculated using the external cross-section of the porous body. Table 2 shows that the flow and peak stresses of all composites decrease as the temperature is increased from room temperature to the melting point of the matrix (660 °C). Above that temperature, the strength of the composites no longer displays significant temperature dependence.

Interconnectivity of the reinforcement has a marked influence on the compressive flow curves of the composites. The first distinguishing feature is the higher flow stress of IPC34 when compared to DRC34, at all temperatures and strains. The relative gain in compressive flow stress $\sigma_{1\%}$ due to interconnection increases with increasing temperature for the present composites, and is 10%, 55% and ca. 89% at 25, 500 and 670 °C, respectively. The second distinguishing feature in the compressive behavior of IPC34 and DRC34 is the respective existence and absence of instabilities in their flow curves. At all temperatures, the stress–strain curves of IPC34 display a peak stress after which the values of stress continuously decrease, unlike DRC34 which exhibits strain hardening at all temperatures. The strain ε_{inst} corresponding to the peak stress of IPC34 decreases with increasing temperature (Table 2). The effect of increasing the volume fraction ceramic in the IPC materials is visible both
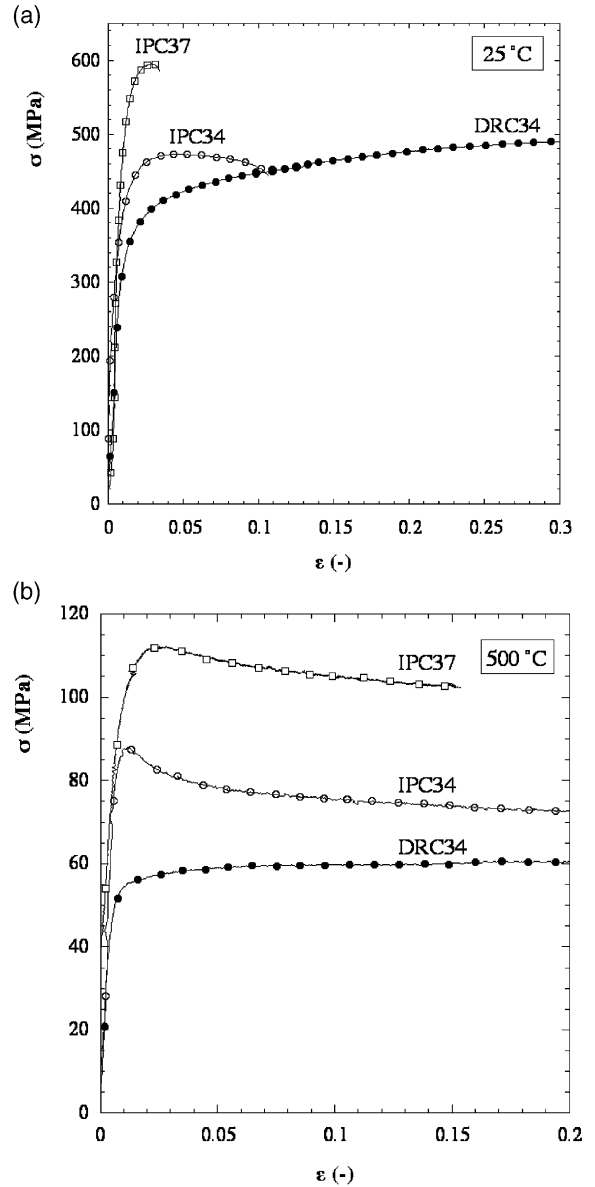

Fig. 2. Typical compressive flow curves of the composites at (a) 25 °C, and (b) 500 °C.

in Fig. 2 and Table 2; IPC37 has a higher compressive flow stress than IPC34 at all temperatures and strains, while the strain at which compressive flow becomes unstable is lower in IPC37 when compared to IPC34 at 25 and 250 °C.

The compressive strength of the ceramic preform (PA34) does not display any significant vari-

Table 2
Measured compressive flow-curve characteristics, strain-rate sensitivity, and rate of damage accumulation

		$\sigma_{1\%}$ [a] (MPa)	$\sigma_{\max}$ [a] (MPa)	$\varepsilon_{\text{inst}}$ [b]	m [40]	n	$dD_1/d\varepsilon$
25 °C	DRC34	356	>495	–	–	0.12	0.15
	IPC34	390	464	0.057	0.010	0.12	1.3
	IPC37	546	595	0.025	0.012	0.12	1.95
250 °C	IPC34	236	284	0.045	0.051	0.07	0.33
	IPC37	326	362	0.02	–	–	–
500 °C	DRC34	55	>60	–	–	0.04	0
	IPC34	85	87	0.015	0.10	0.04	0.12
	IPC37	100	115	0.02	–	0.04	–
600 °C	IPC34	42.5	42.5	0.01	0.10	0.01	–
	IPC37	82	82	0.01	–	0.01	–
670 °C	DRC34	<1	<1	–	–	–	–
	IPC34	[c]	9	<0.01	–	–	–
	IPC37	[c]	19	<0.01	–	–	–
720 °C	IPC34	[c]	7	<0.01	–	–	–

[a] Typical experimental error ± 5%.
[b] Typical experimental error ± 0.01.
[c] Strain at $\sigma_{\max}$ is less than 1%.

ation between room temperature and 670 °C. An average compressive strength of 17 (±2) MPa was determined, which is in good agreement with the correlation between fracture stress and relative density established for open cell alumina foams in Ref. [20].

3.4. Pre-straining effects

As shown in Fig. 3a, the flow stress at 25 °C of an IPC34 sample that was pre-strained at 500 °C to 1.5% strain, is similar to the flow stress of a previously undeformed sample. The same holds for a 1.5% pre-strain at 500 °C followed by testing at 250 °C. On the contrary, for a sample pre-strained at 500 °C to 1.5% and then tested at 670 °C, the stress is lower than for a monotonically compressed sample at 670 °C. Similarly, pre-straining at 25 °C to 5.5% strain lowers the flow stress of the sample when tested at 250 °C compared to that of a monotonically compressed sample at 250 °C, Fig. 3b.

3.5. Evolution of elastic constants

The Young's modulus of all composites was found to decrease with increasing plastic pre-strain, with the rate of stiffness loss increasing with decreasing temperature, Fig. 4a. There is also a slight increase in the elastic Poisson's ratio as a function of pre-strain. This is particularly evident at 25 °C while at higher temperatures the increase is smaller than the experimental scatter (Fig. 4b). A slight decrease in the density of the samples as a function of pre-strain was observed and taken into account for the determination of the Young's modulus and the Poisson's ratio [19]. The void volume fraction accumulated during plastic straining was never greater than 0.5%. The evolution of stiffness with pre-strain is strongly influenced by the interconnectivity of the reinforcement; DRC34 shows a lower rate of stiffness loss than IPC34 at a given temperature (Fig. 4a). For the two IPC samples at 25 °C, an increase in volume fraction
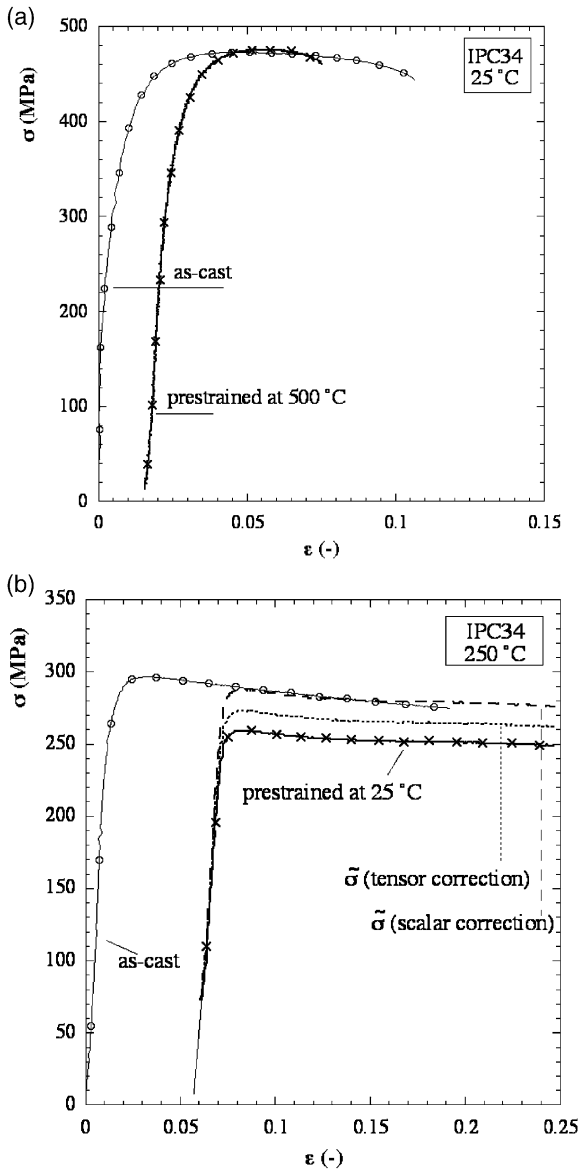
Fig. 3. Effect of pre-straining at temperatures different from the testing temperature on the flow curves of IPC34: (a) pre-straining to 1.5% at 500 °C and testing at 25 °C, and (b) pre-straining to 5.5% at 25 °C and testing at 250 °C. Also shown in (b) are the effective stress–strain curves calculated using two different damage parameters.
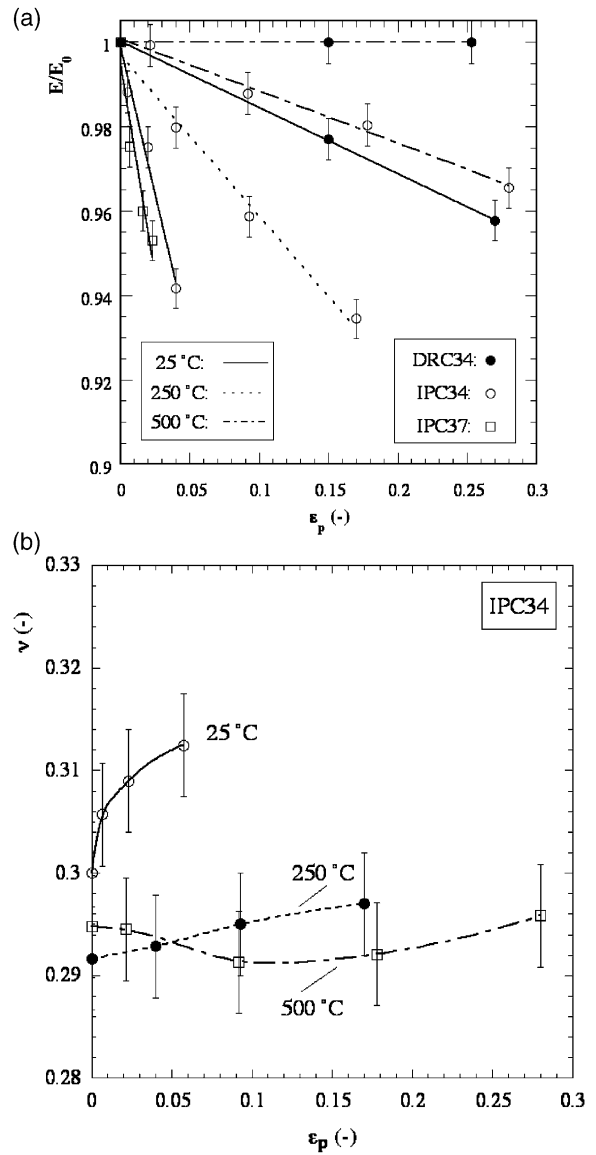

Fig. 4. (a) Relative decrease in ambient-temperature Young's modulus E/E_0 as a function of cumulative plastic strain ε_p and test temperature for DRC34, IPC34, and IPC37. (b) Evolution of Poisson's ratio ν at ambient temperature as a function of ε_p and test temperature for IPC34.

of alumina leads to an increase in the rate of stiffness loss (Fig. 4a).

3.6. Microstructural evolution with strain

Two mechanisms of strain-induced microstructural evolution were observed in IPC34 and IPC37. The first one is the break-up of the interconnected

alumina network, Fig. 5a, which was also examined by dissolution of the aluminum matrix of six IPC34 samples deformed at 25 and 500 °C, to 1%, 2% and 5% strain. In none of these samples was the reinforcement found to be self-supporting after dissolution of the matrix, as it is for samples in the as-cast condition. The alumina powder retrieved after complete dissolution of the matrix was qualitatively examined by SEM. For a given temperature, a greater compressive strain results in a smaller average fragment size in the powder, while for a given strain, a lower testing temperature (and thus a higher stress) results in a smaller size. The

(a)

(b)

Fig. 5. Micrographs illustrating (a) destruction of the interconnected Al_2O_3 network in IPC34 after 5% strain at 600 °C (optical micrograph), and (b) damage in the form of matrix voiding (arrow) in DRC34 after 5% strain at 25 °C (SEM micrograph). Direction of loading is parallel to the scaling bar in both (a) and (b).

fragment size distribution in these retrieved powders was highly non-uniform in all samples, but a statistically significant characterization of the powder size was beyond the scope of this study. The second mechanism of microstructural evolution is the nucleation and growth of matrix voids (Fig. 5b). These voids are preferentially located at particle–matrix interfaces, which are oriented parallel to the axis of applied load, and in areas between particles that are closely spaced in the direction perpendicular to the applied load (Fig. 5b). Matrix cavitation was the only damage mechanism observed in DRC34. The cavities observed in DRC34 are similarly located to those in IPC34, and the fraction of these cavities also appeared to be similar in these two composites. Furthermore, an increase in void volume fraction was noted at lower testing temperatures for all composites.
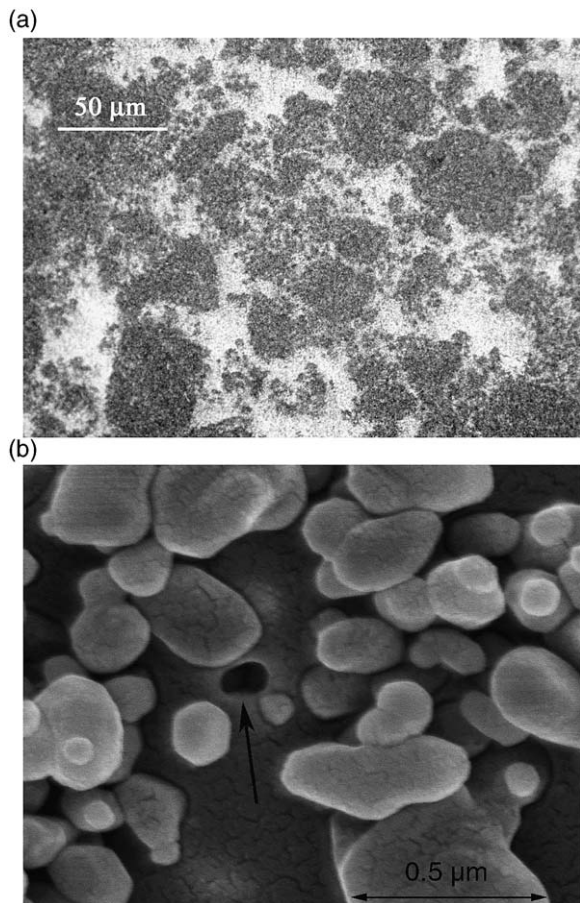
4. Discussion

4.1. Elastic properties

Various models exist to predict the elastic properties of composite materials, although only few focus explicitly on interpenetrating composite microstructures [1]. We consider here two self-consistent approaches, with representative unit cells that capture the basic microstructural differences between IPCs and DRCs. In the first approach, known as the Classical Self-Consistent (CSC) method, both phases of the composite are independently modeled as inclusions within an infinite, homogeneous equivalent continuum that represents the composite [21], as illustrated in Fig. 6b. Interconnectivity of both phases is thus assumed in the CSC approach at all volume fractions, making it a relatively simple analogue of an IPC. In the second approach, known as the Three-Phase Self-Consistent (3PSC) method, each inclusion is surrounded by a layer of matrix, and this assembly of two phases is embedded in the equivalent continuum [21] (Fig. 6b). The microstructure assumed in the 3PSC approach is comparable to that of a DRC, where each reinforcing particle is embedded in the metallic matrix.

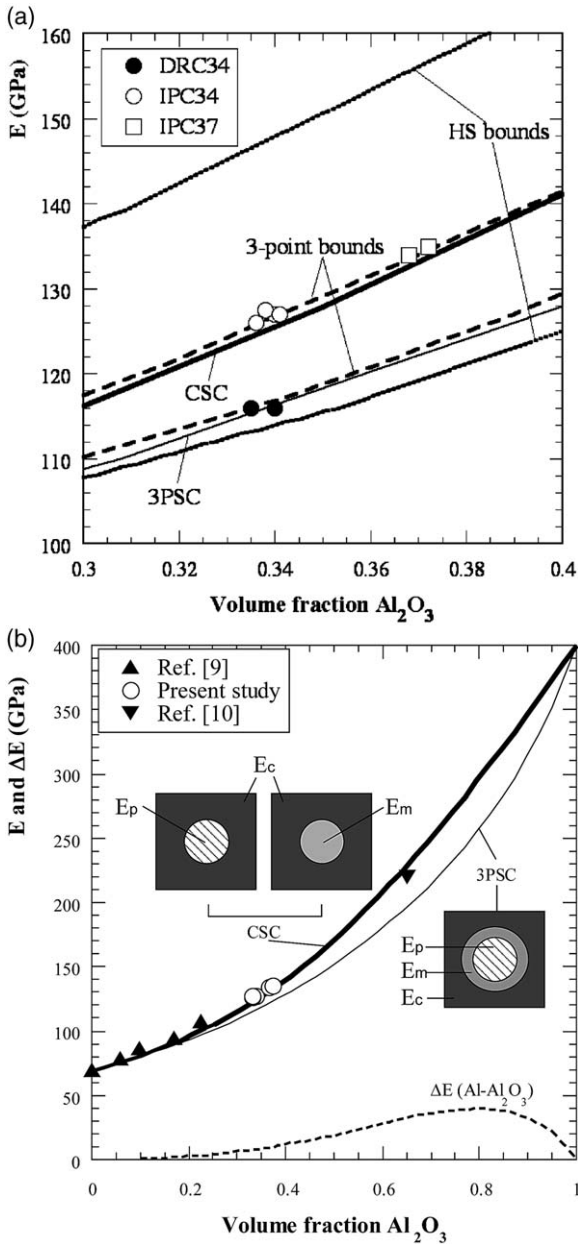Fig. 6a shows the Young's modulus of Al–Al_2O_3

Fig. 6. (a) Young's modulus as a function of Al_2O_3 volume fraction showing predictions of various continuum mechanics models and experimental values. (b) Predictions of the CSC model vs. experimental values of E, for IPCs of this and other studies [9,10]. The relative stiffening of the composites ΔE due to interconnection of the stiffer phase is also shown for the Al–Al_2O_3 system. The representative unit cells for the CSC model and the 3PSC models shown in (b) are from Wilkinson et al. [21].

composites as a function of volume fraction Al_2O_3 as calculated according to the CSC and 3PSC models using the elastic constants of pure Al and Al_2O_3 given in Table 3. Also plotted in Fig. 6a for comparison, are the two Hashin–Shtrikman (HS) bounds [22], and the three-point bounds evaluated for a monodisperse interpenetrating sphere model [23]. The latter bounds are calculated by incorporating statistical information on the phase arrangement of a material through the n-point probability functions, which give the probability of n randomly oriented points all being located within the same phase (the HS bounds in this respect are classified as two-point bounds). For a given volume fraction Al_2O_3, the CSC approach predicts a higher Young's modulus for the composite than the 3PSC approach, as expected, while the solutions for these self-consistent approaches lie between the rigorous HS bounds. In fact, the 3PSC approach and the lower HS bound, both of which assume discrete reinforcements in a contiguous matrix, predict values for the Young's modulus that are close. Predictions of the CSC approach, on the other hand, lie close to those of the upper three-point bound but not the upper HS bound. This is understandable, since the upper HS bound considers the more compliant phase (Al in this case) as

Table 3
Modeling input

(a) Elastic constants

	25 °C	500 °C	25 °C/500 °C
	E (GPa)	E (GPa)	v
Al [45]	69	49	0.345
Al_2O [46]	400	400	0.25

(b) Yield stress and strain hardening exponents for Al matrix

	25 °C		500 °C	
	σ_y (MPa)	n	σ_y (MPa)	n
IPC34 and DRC34	130	0.12	33	0.04
IPC37	170	0.12	[a]	[a]

[a] The stress–strain curve of IPC37 is not modeled at 500 °C since there are no data for the stiffness evolution at this temperature, and thus the experimental curves (to which the model curves are compared) cannot be corrected for damage.

being discretely distributed in a contiguous stiffer phase (Al_2O_3 in this case), and thus considers a microstructure that is not interpenetrating.

The experimentally determined Young's moduli for the composites in this study are also plotted with the model predictions (Fig. 6a). Unlike Table 1, non-averaged values of Young's modulus are presented in Fig. 6a, illustrating typical sample-to-sample scatter. The 3PSC and CSC approaches accurately predict the stiffness (and, thus, the difference in stiffness) of IPC34 and DRC34, respectively. Moreover, the CSC approach accurately predicts the increase in stiffness with increasing volume fraction of alumina for IPC37 with respect to IPC34. The predicted Poisson's ratios are also in reasonable agreement to experimental findings; values of 0.300 and 0.296 were calculated using the CSC model for IPC34 and IPC37 (compared to experimental values of 0.297 and 0.295, Table 1), and 0.314 was calculated using the 3PSC model for DRC34 (compared to 0.320, Table 1). It has been noted previously that the 3PSC approach provides satisfactory predictions for the elastic properties of DRCs [24]. That the CSC approach successfully predicts the elastic properties of IPCs, on the other hand, has so far not been experimentally verified. Stiffness data from the literature for other Al–Al_2O_3 IPCs, at both lower [9] and higher [10] volume fractions of Al_2O_3, Fig. 6b, further substantiate the usefulness of the CSC approach in modelling of IPCs.

The relative increase in stiffness due to interconnectivity of the reinforcement is moderate and amounts to ca. 10%, as illustrated by the Young's moduli of IPC34 and DRC34. This modest increase is due to the relatively small stiffness ratio between the constituents of these composites ($E^{Al_2O_3}/E^{Al}\cong6$). The theoretical increase in stiffness due to interconnectivity of the alumina reinforcement in the Al–Al_2O_3 composite system can be calculated at all volume fractions using the CSC and 3PSC approaches (Fig. 6b). Even at 80 vol.% Al_2O_3 where the stiffening contribution due to interconnectivity of alumina reaches a theoretical maximum, the IPC stiffness is only moderately enhanced with respect to the DRC, Fig. 6b: the relative increase due to interconnectivity is ca. 16%. Assuming, thus, that these continuum mech-

anics models are accurate at all volume fractions, the main contribution to stiffening in the Al–Al_2O_3 system at a given volume fraction, originates from the inherent stiffness of the alumina particles, not their topological characteristics (interpenetrating vs. discontinuous). In order for reinforcement interconnection to become dominant, the stiffness ratio between the composite phases needs to be enhanced [17]. For metal matrix composites, however, stiffness ratios of more than 10 are not usual, so interconnection of the reinforcement provides only a minor contribution to their stiffness.

4.2. Microstructural damage

The main mechanisms of microstructural damage in aluminum composites reinforced with alumina particles larger than 5 µm have been previously identified as reinforcement fracture and matrix cavitation, e.g. Refs. [25–29]; the former mechanism is commonly observed when the particles are larger than ~10 µm, while the latter is more prevalent for smaller particles. In this study, accumulation of voids in the matrix has been observed in all composites, verifying the propensity for matrix cavitation when the reinforcing particles are small (0.3 µm for DSC-Al). Deformation of the IPCs results in the activation of an additional damage mechanism, which is the break-up of their alumina network with increasing strain, qualitatively demonstrated by the matrix-dissolution experiments. The degradation of the alumina network in the IPCs is indirectly quantified by the drop in stiffness with increasing strain at various temperatures (Fig. 4a).

The composite stiffness is more sensitive to damage in the ceramic phase than in the metal matrix, due to the comparatively higher stiffness and, thus, larger load bearing capacity of the ceramic phase. This is evident from the stiffness decrease in DRC34 compared to IPC34 at a given temperature, Fig. 4a; the reinforcement in DRC34 is not significantly damaged during straining, resulting in a relative decrease in its stiffness that is much smaller than the relative decrease in stiffness for IPC34, in which degradation of the interconnected alumina occurs from the onset of deformation. At all strains up to its failure, however, the

absolute stiffness of IPC34 is higher than the initial stiffness of DRC34; the break-up of the ceramic network is a continuous process in strain, and the magnitude of strain that can be imposed prior to failure during uniaxial compression is not sufficient to completely break up this network, unlike during extrusion.

The rate of damage accumulation (i.e. the slope of the stiffness vs. strain curves in Fig. 4a) decreases with increasing temperature for all composites. Also, an increase in temperature results in a decrease of composite stress, Fig. 2, due to the strong temperature dependence of the flow stress in the aluminum matrix. At higher temperatures, thus, the stress in both the matrix and the reinforcement is lower, reducing the propensity for both matrix voiding and damage of the alumina network, evident in the comparison of the rate of damage accumulation at 25 and 500 °C of DRC34 and IPC34, respectively (Fig. 4a). That the accumulation of damage is not exclusively related to strain or stress alone has been noted in prior studies on composites reinforced with larger ceramic particles than the present materials [24,25].

The accumulation of damage affects not only the stiffness but also the flow properties of the composites, as can be seen by comparing the flow curves of IPC34 and DRC34 at the same temperature (Fig. 2). As damage progresses, the rate of strain hardening of IPC34 continuously decreases up to a critical (temperature-dependent) strain, after which it becomes negative. DRC34, on the other hand, which accumulates damage at a much lower rate as compared to IPC34, does not exhibit strain softening. Previous studies on particle-reinforced aluminum have shown that the damage-corrected stress or effective stress, $\tilde{\sigma}$, can be related to the measured true stress, σ, as:

$$\tilde{\sigma} = \frac{\sigma}{1-D} \qquad (1)$$

where D is an appropriate damage parameter [24,30]. In particular, the scalar damage parameter D_1 derived from the strain equivalence postulate of continuum damage mechanics, and based on the relative decrease in stiffness, was shown [24] to be a good damage descriptor for metal matrix-composites:

$$D_1 = 1 - \frac{E}{E_0} \qquad (2)$$

where E_0 and E, are the Young's moduli of the composite before deformation and after a specific strain increment, respectively. Microstructural damage was thus shown to affect the flow stress and the stiffness of particle reinforced aluminum in a similar way.

The effect of damage on the flow stress of the present composites is further demonstrated by the pre-straining experiments; reloading IPC34 after pre-straining at a lower temperature, results in a lower flow stress compared to continuous deformation at the testing temperature (Fig. 3b). Since damage accumulates at a higher rate during deformation at lower temperatures, Fig. 4a, additional microstructural damage accumulated during the initial low temperature deformation explains the reduction of the flow stress at higher temperatures. The effective stress–strain curve of IPC34 at 250 °C, after pre-straining at 25 °C, can be calculated so as to take into account the pre-strain damage. Using the data of Fig. 4a for IPC34 at 25 °C, Eq. (2) is used to calculate the value of D_1 at 5.5% strain—the amount of pre-strain at 25 °C. The effective stress at 250 °C is then calculated using Eq. (1) and compared to the monotonically strained sample at 250 °C (Fig. 3b). It should be noted that the continuous damage occurring in both pre-strained and monotonically strained samples at 250 °C is not accounted for in Fig. 3b; taking it into account—as above using the data of Fig. 4a—produces an upwards shift of the same magnitude in the stress–strain curves of the monotonically deformed and pre-strained curves. The damage-corrected curve of the pre-strained sample is almost identical to the monotonically deformed sample, ascertaining the utility of Eqs. (1) and (2) in determining a damage-corrected flow stress in agreement with previous studies on composites reinforced with discrete reinforcements.

In spite of the successful prediction of the effective stress, the strain equivalence postulate remains a simplification of reality. The fact that the Poisson's ratio does not remain constant, Fig. 4b, as the stiffness decreases and, thus, damage progresses, is an indication that damage is not isotropic, which

is an implicit assumption for the use of a scalar damage parameter. An energy equivalence postulate has been proposed [31] to account for anisotropic damage, resulting in a third order damage tensor. The D_{11} component of this tensor is of interest for uniaxial loading and has the form:

$$D_{11} = 1 - \sqrt{\frac{E}{E_0}} \tag{3}$$

We calculate the effective stress–strain curve in Fig. 3b in the same manner as above, but using D_{11} instead of D_1. When using D_{11} as a damage parameter, the effective stress–strain curve is lower, as expected, and the agreement between experimentally measured and effective curves is not as good.

Anisotropic damage has been observed in previous studies of DRCs containing coarse reinforcements (>10 μm); particles tend to fracture along planes perpendicular to the principal tensile axis, which in tension are perpendicular to the loading axis and in compression parallel to the loading axis [32]. In the present study, the Poisson's ratio of IPCs tested at room temperature increases as deformation proceeds (Fig. 4b), indicating a greater loss in lateral than longitudinal constraint as damage proceeds. This implies that microcracks are oriented parallel to the compression axis as in DRCs. The evolution of the Poisson's ratio is modest, however, at 25 °C and negligible at 250 and 500 °C. The scalar damage parameter can thus be considered a sufficient approximation for the present uniaxial loading conditions [33]. In fact, it captures the effect of damage on the flow stress better than a tensor damage parameter, as shown in Fig. 3b. If, however, more complex loading histories were to be studied, damage-induced anisotropy would have to be considered using a different postulate than those of strain and elastic energy equivalence.

4.3. Composite flow curves

The influence of reinforcement interconnectivity on the elastic properties of the composites was demonstrated by using the CSC and 3PSC models (Fig. 6a and b). These models are also used to understand the influence of interconnectivity on the

plastic behavior of the IPCs. In the following, the role of damage is eliminated by considering the effective flow curves, i.e. the flow curves corrected for damage using the damage parameter D_1, calculated from the stiffness-decrease data of Fig. 4a. Also, dispersion strengthening—due to the interaction of dislocations with the sub-micron particles at low strain rates where dislocation climb is dominant [34]—is assumed negligible at the high strain rates (and stresses) used in the present study where dislocation glide is dominant.

The volume fraction of Al_2O_3 for these calculations is set to 0.34 for IPC34 and DRC34, and 0.37 for IPC37. The constitutive equation of the ceramic is assumed to be linearly elastic and temperature-independent, as supported by compressive testing of Al_2O_3 preforms (PA34), which show no significant change in mechanical response between 25 and 670 °C. The constitutive response of the aluminum is described by the Ramberg–Osgood equation:

$$\varepsilon = (\sigma/E_m) + \alpha(\sigma_y/E_m)(\sigma/\sigma_y)^{1/n} \tag{4}$$

where ε is the strain, E_m is the temperature dependent Young's modulus, α is a dimensionless constant equal to 3/7, σ_y is the yield strength and n is the strain-hardening coefficient. As listed in Table 2, E_m is calculated according to Ref. [35], n is set equal to the effective composite strain-hardening coefficient determined experimentally [36,37], and σ_y is numerically optimized to give the best-fit between calculated and experimental curves. To apply the CSC and 3PSC approaches to the nonlinear problem of plasticity, the aluminum behavior is linearized past its yield point using the secant modulus approximation. The stress–strain relationship of IPC34, IPC37 and DRC34 is calculated based on these constitutive properties, the equations developed for the CSC model in Ref. [38] and the 3PSC model in Ref. [39], and an incremental numerical procedure outlined in Table 1 of Ref. [38].

The results of the calculations are presented in Fig. 7a and b, for 25 and 500 °C. We limit the following discussion to the effects of interconnectivity on the flow properties of the composites, i.e. to a comparison of IPC34 and DRC34; in the last section of the discussion, we comment on the
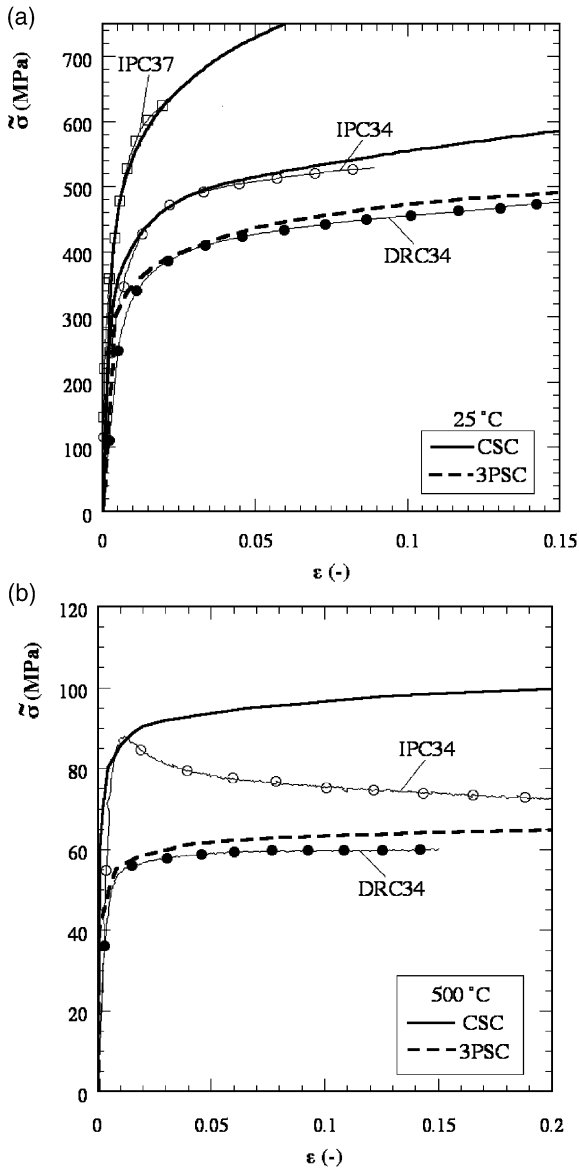
(a)

(b)

Fig. 7. Effective flow curves of the composites (i.e. corrected for damage) compared to model predictions at (a) 25 °C, and (b) 500 °C.

differences between IPC34 and IPC37. At 25 °C, the agreement between computed and effective flow curves is good for both IPC34 and DRC34. At 500 °C, this is true for DRC34 only, because IPC34 exhibits a flow instability at ~1% strain, which cannot be taken into account by the damage correction alone, as discussed in the next section.

The agreement between model and experiment for IPC34 at 500 °C is satisfactory at strains smaller than 1%. The significance of this agreement, however, lies in the modeling input presented in Table 3; at both temperatures, the experimental flow curves for IPC34 and DRC34 are reproduced by inputting the same material parameters into the CSC and the 3PSC models, respectively. Thus, these calculations show that, at a given volume fraction of reinforcement, the difference in reinforcement topology can fully account for differences in the measured composite flow stresses. The values of σ_y for the aluminum matrix used in the calculations, Table 3, are higher than their respective handbook values for bulk aluminum, even in its cold-worked state. This enhancement in the in situ flow properties of the aluminum matrix is due to indirect strengthening provided by the particles in the form of forest dislocation hardening, which is independent of the direct strengthening due to load-partitioning examined here, and is discussed in more detail in another publication [40].

With increasing temperature, the relative increase in strength due to interconnection of the particles becomes more important, making IPC34 an interesting material for high temperature applications as compared to DRC34 (this is true for strains below 1% due to flow instabilities). The role of the reinforcement as a load-bearing element in metal matrix composites becomes increasingly important as temperature increases, for both interpenetrating and non-interpenetrating microstructures. This is due to the increase in the mismatch between the mechanical properties of their constituents at higher temperatures, which results in the reinforcement carrying a relatively larger proportion of the composite stress [41]. In IPCs, the interconnected ceramic phase invariably carries a larger proportion of the composite stress when compared to the discontinuous particulate in DRCs, enhancing the difference between room-temperature and high-temperature properties. To illustrate this point, the CSC and 3PSC models were applied to determine the fraction of the composite stress carried by the ceramic phase in IPC34 and DRC34, at 25 and 500 °C, and at the reference strain of 1%. For IPC34, ca. 62% of the composite

stress is borne by the ceramic phase at 25 °C, compared to 70% at 500 °C. For DRC34, on the other hand, ca. 54% of the composite stress is carried by the ceramic particles at 25 °C, and this number only slightly increases at 500 °C, to 55%. The benefit of an interconnected ceramic reinforcement in a reinforced metal, thus, becomes more significant at higher temperatures. Testing the composites at 670 °C demonstrates this point at the limit of an infinite mismatch in mechanical properties: the maximum stress of IPC34 (9 MPa) is close to that of preform PA34 (17 MPa) since the molten aluminum matrix cannot transmit any load to the reinforcement. DRC34, on the other hand, exhibits a flow stress less than 1 MPa at this temperature.

4.4. Instability strain

Previous studies have shown that an increased rate of damage accumulation in DRCs lowers the strain at which flow instabilities occur during room-temperature tension testing [24,42]. Similar trends are observed here for room-temperature compression of the IPC materials; IPC37 accumulates damage at a higher rate than IPC34, Fig. 4a, and has a lower instability strain (Fig. 2a). At elevated temperatures, however, an additional factor influencing the development of instabilities must also be considered, i.e. strain-rate sensitivity, which increases with increasing temperature for these IPCs [40].

Following the Hart analysis for power-law hardening in both strain and strain rate [43], and for tests conducted at constant crosshead speed, the instability strain ε_{inst} at elevated temperatures can be expressed as:

$$\varepsilon_{inst} = \frac{n}{1 + m} \qquad (5)$$

where m is the strain rate sensitivity parameter [43]. For composite materials that accumulate microstructural damage, however, it is the effective stress that displays power-law hardening, rather than the measured stress, as shown in Fig. 7 and reported in Ref. [24]. Substituting the true stress with the effective stress in the Hart analysis (as was done in the Considere analysis of room-tem-

perature instability in Ref. [24]) results in an instability strain of the form:

$$\varepsilon_{inst} = \frac{n}{1 + m - \dfrac{d\ln(1-D)}{d\varepsilon}} \qquad (6)$$

Eq. (6) is the general form for the onset of flow instabilities in materials that accumulate microstructural damage and are strain-rate sensitive, during compression testing at a constant crosshead speed.

Experimentally determined instability strains are plotted in Fig. 8 with the solutions of Eq. (6), showing good agreement; the experimental values for n (determined from power-law fits to the effective composite stress–strain curves, Fig. 7), $dD/d\varepsilon$ (Fig. 4a), and m (from a companion study, Ref. [40]) are given in Table 2. The dotted line in Fig. 8 delineates the limit as damage goes to zero, showing the effect of n and m in the absence of damage. Damage accumulation (illustrated by the full lines in Fig. 8) is greatest at low temperatures, where it significantly reduces the instability strain, but it plays almost no role at high temperatures. The strain sensitivity parameter m is greater at high
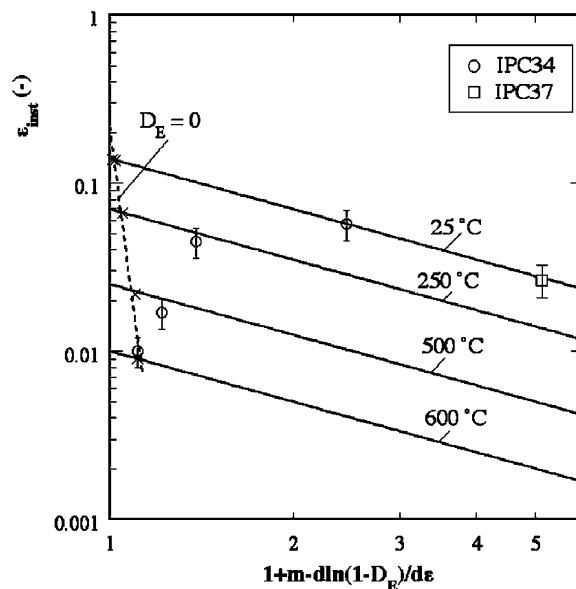

Fig. 8. Comparison between experimental data and Eq. (6) linking the rate of damage accumulation and the strain-rate sensitivity parameter to the instability strain.

temperatures, but this does not substantially reduce the onset of non-uniform flow (rather it tends to stabilize non-uniform deformation past the instability strain [43]). It is primarily the decrease in *n* with temperature that leads to the significant reductions in instability strain at high temperatures.

This instability analysis is a necessary but not sufficient condition for the development of compressive flow instabilities. Eq. (6) predicts the strain at which flow becomes localized, and hence unstable, as in the IPCs. Localized flow, however, may not develop as is the case in DRC34. This difference in compressive flow stability cannot be attributed to differences in lubrication of the compression platen–sample interface or machine alignment, since all tests were performed under similar conditions with the same sample geometry and the results were reproducible. The only factor that differentiates the IPCs and DRC is their microstructure, which is a parameter known to affect compressive flow instabilities in unreinforced metals [43]. Reinforcement interconnectivity in IPCs results not only in accelerated damage accumulation but also is responsible for the initiation of flow instabilities in compression. This has direct implications for the formability of these composites; IPCs may not be easily formed by conventional metal forming operations due to the early localization of strain, while DRCs are expected to be more resistant to forming instabilities.

4.5. Effect of reinforcement volume fraction on metal matrix IPCs

The stiffness and compressive flow stress of metal matrix composites are enhanced by higher volume fractions of the stiffer reinforcement, except perhaps when damage is significantly accelerated so as to cause premature failure. Comparison of the flow behavior for IPC34 and IPC37 shows this trend at all temperatures (Fig. 2 and Table 2). Based solely on a continuum mechanics approach (and ignoring dislocation–particle interactions which become dominant at low strain rates [34]), it is expected that the increase in the elasto-plastic property mismatch between phases with increasing temperature would tend to enhance the strengthening offered by the interconnected

reinforcement, and that this difference would be more pronounced in IPC37 than IPC34 due to its larger volume fraction ceramic [15]; this would result in a relative increase in strength of IPC37 with respect to IPC34, that becomes more pronounced with increasing temperature. However, the relative increase in flow stress of composite IPC37 with respect to IPC34 is smaller at 500 °C than at 25 °C (18% vs. 40% for the stress at 1% strain). A probable reason for this discrepancy is that the in situ properties of the aluminum matrix are substantially altered by the presence of the reinforcement, as compared to bulk aluminum. The aluminum matrix is hardened by mismatch dislocations generated during cool-down from processing temperatures (because of the thermal expansion difference between the metal matrix and the ceramic particles [34,37,44]), and during deformation up to 1% strain (because of elasto-plastic mismatch). The higher the volume fraction of particles, the greater the density of these mismatch dislocations, resulting in a higher in situ matrix yield stress in IPC37 compared to IPC34 (Table 3). As the testing temperature is increased, mismatch dislocations tend to annihilate thus decreasing the relative difference in in situ yield stress between the matrices of IPC37 and IPC34, and explaining the trend in the relative stress increase for IPC37 and IPC34 with temperature. The effect of these mismatch dislocations on the micro-mechanisms of deformation in the present materials is treated in detail elsewhere [40].

5. Conclusions

The effect of reinforcement interconnectivity was studied in aluminum composites containing sub-micron alumina particles produced by liquid metal infiltration. At room temperature and for a volume fraction of 34% Al_2O_3, the IPC offers only moderate relative increases in stiffness and flow stress as compared to the DRC. Both the elastic and plastic behavior of these composites can be successfully modeled using a self-consistent approach: the IPC and DRC microstructures are idealized by the CSC and the 3PSC models, respectively. These models predict that, even at 80

vol.% Al_2O_3 where the contribution due to interconnectivity of alumina is at a theoretical maximum, an interconnected architecture offers only a modest increase in room-temperature stiffness as compared to a discontinuous structure.

At elevated temperatures, the interconnected reinforcement becomes increasingly more effective at strengthening the composite, due to the enhanced mismatch in the mechanical properties of aluminum and alumina. This benefit, however, can be utilized only at small strains due to the early development of compressive flow instabilities in the IPCs. Accumulation of microstructural damage reduces the instability strain of the IPCs at room temperature; however, at elevated temperatures the instability strain is reduced primarily as a result of the low strain-hardening coefficient of the composites.

In summary, moderately enhanced mechanical properties at room temperature and attractive high temperature properties are the benefits of an interconnected architecture (as compared to a discontinuous architecture) for the ceramic reinforcement of metal matrix composites. The disadvantages are accelerated damage accumulation and the development of flow instabilities at all temperatures.

Acknowledgements

References

[1] Gilormini P, Bréchet Y. Model Simul Mater Sci Eng 1999;7:805.
[2] Shen Y-L, Finot M, Needleman A, Suresh S. Acta Metall Mater 1994;42:77.
[3] Christman T, Needleman A, Suresh S. Acta Metall 1989;37:3029.
[4] Prangnell PB, Barnes SJ, Roberts SM, Withers PJ. Mater Sci Eng 1996;42:41.
[5] Murphy AM, Howard SJ, Clyne TW. Mater Sci Technol 1998;14:959.
[6] Clarke DR. J Am Ceram Soc 1992;75(4):739.
[7] Knechtel M, Prielipp H, Müllejans H, Claussen N, Rödel J. Scripta Metall Mater 1994;31(8):1085.
[8] Breslin MC, Ringnalda J, Xu L, Fuller M, Seeger J, Daehn GS et al. Mater Sci Eng 1995;A195:113.
[9] Peng HX, Fan Z, Evans JRG. Mater Sci Eng 2001;A303:37.
[10] Daehn GS, Starck B, Xu L, Elfishawy KF, Ringnalda J, Fraser HL. Acta Mater 1996;44:249.
[11] Prielipp H, Knechtel M, Claussen N, Streiffer SK, Müllejans H, Rühle M et al. Mater Sci Eng 1995;A197:19.
[12] Hoffman M, Skirl S, Pompe W, Rödel J. Acta Mater 1999;47:565.
[13] Pezzotti G, Suenobu H, Nishida T. J Am Ceram Soc 1999;82(5):1257.
[14] Zimmermann A, Hoffman M, Emmel T, Gross D, Rödel J. Acta Mater 2001;49:3177.
[15] Wegner LD, Gibson LJ. Int J Mech Sci 2000;42:925.
[16] Wegner LD, Gibson LJ. Int J Mech Sci 2000;42:943.
[17] Wegner LD, Gibson LJ. Int J Mech Sci 2000;43:1061.
[18] Brown AM, Klier EM. US Patent No 5,511,603; 1996.
[19] Schreiber E, Anderson OL, Soga N. Elastic constants and their measurement. New York: McGraw-Hill, 1973.
[20] Goretta KC, Brezny R, Dam CQ, Green DJ, De Arellano-Lopez AR, Dominguez-Rodriguez A. Mater Sci Eng 1990;A124:151.
[21] Wilkinson DS, Pompe W, Oeschner M. Prog Mater Sci 2001;46:379.
[22] Hashin Z, Shtrikman S. J Mech Phys Solids 1962;10:335.
[23] Torquato S. Appl Mech Rev 1991;44(2):37.
[24] Kouzeli M, Weber L, San Marchi C, Mortensen A. Acta Mater 2001;49:3699.
[25] Lloyd DJ. Acta Metall Mater 1991;39:59.
[26] Singh PM, Lewandowski JJ. Metall Trans 1993;24A:2531.
[27] Mummery PM, Derby B. J Mater Sci 1994;29:5615.
[28] Sinclair I, Gregson PJ. Mater Sci Technol 1997;13:709.
[29] Kouzeli M, Weber L, San Marchi C, Mortensen A. Acta Mater 2001;49:497.
[30] Poole WJ, Dowdle EJ. Scripta Mater 1998;39(9):1281.
[31] Skrzypek JJ, Ganczarski A. Modeling of material damage and failure of structures. Berlin: Springer, 1999.
[32] Hong SI. Scripta Mater 1999;4(4):433.
[33] Lemaître J, DesMorat R. In: Lemaître J, editor. Handbook of materials: behavior models. San Diego: Academic Press; 2001. p. 513–24.
[34] Jansen AM, Dunand DC. Acta Mater 1997;45:4583.
[35] Frost HJ, Ashby MF. Deformation-mechanism maps. In: The plasticity and creep of metals and ceramics. Oxford: Pergamon Press, 1982.
[36] Bao G, Hutchinson JW, McMeeking RM. Acta Metall Mater 1990;39:1871.
[37] Kouzeli M, Mortensen A. Acta Mater 2002;50:39.
[38] Corbin SF, Wilkinson DS. Acta Metall Mater 1994;42:1311.
[39] Christensen RM. In: Mechanics of composite materials. Wiley-Interscience; 1979. p. 32–58.
[40] Kouzeli M, Dunand DC. Effect of temperature and strain-

rate on the compressive flow of al composites containing sub-micron Al_2O_3 particles. Metall Mater Trans, in press.

[41] Daymond MR, Lund C, Bourke MAM, Dunand DC. Metall Mater Trans 1999;30A:2989.

[42] Kiser MT, Zok FW, Wilkinson DS. Acta Mater 1996;44:3465.

[43] Semiatin SL, Jonas JJ. Formability and workability of metals. In: Plastic instability and flow localisation. Metals Park (OH): ASM, 1984.

[44] Humphreys FJ. In: Andersen SI, Lilholt H, Pedersen OB, editors. 9th Risø International Symposium on Metallurgy and Materials Science. Roskilde (Denmark): Risø National Laboratory; 1988. p. 51.

[45] Boyer HE, Gall TL, editors. Metals handbook. desk edition. Metals Park (OH): ASM International; 1985.

[46] Shneider SJ, editor. Engineered materials handbook. Ceramics and glasses, vol. 4. Metals Park (OH): ASM International; 1991.